

# Radiative feedback and cosmic molecular gas: numerical method

Margarita Petkova<sup>1,2\*</sup>, Umberto Maio<sup>3†</sup>

<sup>1</sup> *University of Bologna, Department of Astronomy, via Ranzani 1, I-40127 Bologna, Italy*

<sup>2</sup> *Max-Planck-Institut für Astrophysik, Karl-Schwarzschild-Straße 1, D-85748 Garching b. München, Germany*

<sup>3</sup> *Max-Planck-Institut für extraterrestrische Physik, Giessenbachstraße 1, D-85748 Garching b. München, Germany*

(draft)

## ABSTRACT

We present results from self-consistent numerical simulations of cosmic structure formation with a multi-frequency radiative transfer scheme and non-equilibrium molecular chemistry of 13 primordial species ( $e^-$ , H,  $H^+$ ,  $H^-$ , He,  $He^+$ ,  $He^{++}$ ,  $H_2$ ,  $H_2^+$ , D,  $D^+$ , HD,  $HeH^+$ ), performed by using the simulation code GADGET. We describe our implementation and show tests for ionized sphere expansion in a static and dynamic density field around a central radiative source, and for cosmological abundance evolution coupled with the cosmic microwave background radiation. As a demonstrative application of radiative feedback on molecular gas, we run also cosmological simulations of early structure formation in a  $\sim 1$  Mpc size box. Our tests agree well with analytical and numerical expectations. Consistently with other works, we find that ionization fronts from central sources can boost  $H_2$  fractions in shock-compressed gas. The tight dependence on  $H_2$  lead to a corresponding boost of HD fractions, as well. We see a strong lowering of the the typical molecular abundances up to several orders of magnitudes which partially hinders further gas collapse of pristine neutral gas, and clearly suggests the need of re-ionized gas or metal cooling for the formation of the following generation of structures.

**Key words:** cosmology: theory – structure formation

## 1 INTRODUCTION

The preset understanding of cosmic structure formation relies on the observations of a Universe expanding at a rate of  $H_0 \simeq 70$  km/s/Mpc and whose energy budget is largely dominated by a form of unknown ‘dark’ energy or cosmological constant,  $\Lambda$ , that contributes  $\sim 70\%$  to the total cosmic energy content. The residual matter contribution is roughly  $\sim 30\%$ , but only a very small fraction of  $\sim 4\%$  consists of ordinary baryonic matter, while the rest is unknown cold (i.e. non-relativistic) ‘dark matter’ (DM). More precisely, recent determinations suggest  $\Omega_{0,m} = 0.272$ ,  $\Omega_{0,\Lambda} = 0.728$ , and  $\Omega_{0,b} = 0.044$  (Komatsu et al. 2011). In this framework, also called  $\Lambda$ CDM model, cosmological structures can grow from gravitational instability (Jeans 1902) of primordial matter fluctuations, probably originated during the primordial inflationary epoch. These early perturbations represent the seeds which would develop into present-day galaxies and stars (Schwarzschild & Spitzer 1953) by gas cooling and condensation (Spitzer 1962), and they will affect the surround-

ing environment through a number of mechanical, chemical and radiative processes commonly known as feedback effects (on this topic, see the extensive review by Ciardi & Ferrara 2005).

Quantitatively speaking, linear perturbation analyses are usually performed to study the initial phases of gravitational collapse, where a Gaussian density distribution for the primordial matter fluctuations is assumed. The linear expansion of the continuity, Euler, and energy equations can also be extended with higher-order corrections (e.g. Tseliakhovich & Hirata 2010; Maio et al. 2011; Stacy et al. 2011; Greif et al. 2011) or non-Gaussian deviations (e.g. Grinstein & Wise 1986; Koyama et al. 1999; Komatsu et al. 2002; Grossi et al. 2007; Desjacques et al. 2009; Maio & Iannuzzi 2011; Maio 2011; Maio & Khochfar 2012), but to study non-linear regimes and feedback mechanisms it is essential to perform numerical integrations and use N-body/hydro simulations. Indeed, to capture early gas collapse it is needed not only to follow gravity and hydrodynamics, but also its full chemistry evolution and molecule formation. Since in the cosmic medium hydrogen (H) is the most abundant species with a cosmological mass fraction of  $X_H \simeq 0.76$  (corresponding to  $\sim 0.93$  in number fraction), its contribution in gas

\* E-mail: margarita.petkova@unibo.it

† E-mail: umaio@mpe.mpg.de

cooling is likely to play a very relevant role, together with helium (He). However, H and He collisional processes are able to cool the medium to  $\sim 10^4$  K via resonant line transitions, but they are not capable to bring the gas temperature further down. At such low temperatures, thermal collisions are not able to excite the electrons to higher levels due to the large energy gaps (from a few to some tens of eV) of H and He atomic configurations. Saslaw & Zipoy (1967) proposed that gas cooling and fragmentation could be continued below  $\sim 10^4$  K by H<sub>2</sub> cooling, down to  $\sim 10^2 - 10^3$  K. Later, Lepp & Shull (1984) suggested that the existence of primordial deuterium (D) could determine HD formation and consequent cooling even below  $\sim 10^2$  K, down to several  $\sim 10$  K. During the last decades, these problems have been tackled by collecting full reaction networks (Shapiro & Kang 1987a; Puy et al. 1993; Galli & Palla 1998; Hui & Gnedin 1997a; Abel et al. 1997; Uehara & Inutsuka 2000; Nakamura & Umemura 2002; Omukai et al. 2005; Glover & Abel 2008; Omukai et al. 2010; Glover et al. 2010) and by running high-resolution chemistry cosmological simulations, both in the standard  $\Lambda$ CDM model (e.g. Abel et al. 2002; Bromm et al. 2002; Yoshida et al. 2003, 2007) and in dark-energy cosmological models (Maio et al. 2006). Further on, the effects of metal cooling have been investigated in numerical simulations by joining molecular chemistry evolution with metal pollution and low-temperature fine structure transitions from, e.g., C, O, Si, Fe (e.g. Maio et al. 2007). These studies clearly show the strong implications of metals on the cosmological chemical evolution (chemical feedback) and how the rapidity of early enrichment from first star formation episodes (see also Tornatore et al. 2007) overcomes gas molecular cooling (Maio et al. 2010, 2011), marking the transition from the primordial, pristine star formation regime - i.e. the so-called population III (popIII) regime - to the more standard population II-I (popII-I) regime (Maio et al. 2010). This transition is often parameterized in terms of a minimum critical metallicity  $Z_{crit} \sim 10^{-4} Z_{\odot}$ , but given our ignorance about early dust production and detailed atomic and molecular data,  $Z_{crit}$  has large uncertainties: its expected value varies between  $\sim 10^{-6} Z_{\odot}$  (Schneider et al. 2003) -  $10^{-5} Z_{\odot}$  (Omukai et al. 2010) and  $\sim 10^{-3} Z_{\odot}$  (Bromm & Loeb 2003). There are also recent arguments on the possible existence of a critical dust-to-gas ratio (Schneider et al. 2012).

Once the first stars are formed, they shine and emit radiation. This can have relevant impacts (radiative feedback) (Efstathiou 1992) on the surrounding medium and on the following star formation history (e.g. Ciardi et al. 2000, 2001; Whalen et al. 2004; Iliev et al. 2005; Alvarez et al. 2006; Susa & Umemura 2006; Iliev et al. 2006, 2009; Whalen et al. 2010; Mellema et al. 2006; Susa et al. 2009; Gnedin et al. 2009; Petkova & Springel 2011; Paardekooper et al. 2011; Wolcott-Green et al. 2011). Therefore, appropriate radiative transfer (RT) calculations coupled with hydrodynamics and chemistry must be performed in order to consistently explore the repercussions on molecule destruction or enhancement, and hence on structure formation in the early Universe. There have been studies on how the radiation feedback affects larger halos such as clusters and galaxies (e.g. Shapiro et al. 2004; Yoshida et al. 2007; Croft & Altay 2008), and particular interest has arisen from popIII stars (Wise & Abel 2008; Hasegawa et al. 2009; Smith et al. 2009; Whalen et al. 2010), whose large luminosities (which suggest them as pro-

genitors of early gamma-ray bursts, e.g. Campisi et al. 2011; de Souza et al. 2011; Campisi et al. 2011) not only ionize, but also expel gas from the pristine mini-halos they sit in. For example, Lyman-Werner photons (11.2 - 13.6 eV) at early times could eradicate H<sub>2</sub> from halos, delaying or completely impeding the collapse of molecular gas (e.g. Susa 2007; Wise & Abel 2007; Johnson et al. 2007; Ahn et al. 2009; Trenti & Stiavelli 2009; Whalen et al. 2010). Non the less, several issues in this respect are still unsolved, like the role of radiative feedback on popIII star formation, its efficiency in halting or boosting gas cooling in primordial environment, its interplay with mechanical and chemical feedback, its effects on the dynamical and thermodynamical state of the cosmic gas, or its connections to the set-up of a turbulent medium dominated by hydro-instabilities (e.g. Maio et al. 2011).

First semi-analytical works (Haiman et al. 1997a,b; Haiman 1999) expected molecular hydrogen to be universally destroyed by UV stellar radiation in the LW band.

Subsequent, one-dimensional, numerical studies of small- or intermediate-size boxes ( $< 1$  Mpc a side), including RT coupled with hydrodynamics, demonstrated that these predictions were overestimating molecular destruction, and, despite the stellar UV radiation, H<sub>2</sub> could be rapidly reformed in the shock compressed gas of the ionization fronts (I-fronts) of HII regions (Ricotti et al. 2001, 2002a,b, showed that via a Softened Lagrangian Hydrodynamics Particle-Particle-Mesh, SLH-P<sup>3</sup>M, implementation). This was the first suggestion for “positive” feedback exerted by I-fronts on primordial structure formation.

Similar calculations applied to individual haloes nearby primordial stellar sources (e.g. Shapiro et al. 2004; Iliev et al. 2005; Hasegawa et al. 2009) showed that UV radiation from popIII stars in crowded star forming regions could photoevaporate small ( $\sim 10^7 M_{\odot}$ ) haloes in  $\gtrsim 100$  Myr. However, more recent studies (e.g. Susa & Umemura 2006; Susa et al. 2009; Hasegawa et al. 2009; Whalen et al. 2008; Whalen & Norman 2008; Whalen et al. 2010) found that halo photoevaporation due to first stars strongly depends on the features of the stellar sources and on the hydrodynamical properties of the collapsing cloud. Thus, radiative feedback was found to be able to trigger gas cooling by catalyzing H<sub>2</sub> formation. In order to overcome numerical issues in larger cosmological simulations ( $\gtrsim 1$  Mpc a side), further studies adopted simple analytical prescriptions for a mean, *uniform*, UV background, assumed to be established after the early onset of star formation (e.g. Machacek et al. 2001, 2003; Mesinger et al. 2006, 2009, via a grid Adaptive Mesh Refinement, AMR, implementation). In the same spirit, detailed, AMR, popIII, star formation calculations in *uniform* LW backgrounds (O’Shea & Norman 2008a; Wise & Abel 2008; Shang et al. 2010) confirmed that the LW background is much less destructive to new popIII stars than originally supposed, and, even by assuming extremely high background values of  $J \geq 10^{-21} \text{ erg s}^{-1} \text{ cm}^{-2} \text{ Hz}^{-1} \text{ sr}^{-1}$  ( $\equiv J_{21}$ ) star formation is just delayed, not shut down.

This essential review shortly shows how debated the issues related to radiative feedback are and highlights the numerous unknowns when dealing with RT and molecular chemistry. In the present work, we aim at contributing to the scientific discussions and works already existing in literature by implementing three-dimensional RT schemes fully cou-

pled with hydrodynamics, and non-equilibrium chemistry. At the end of the paper, together with chemistry and radiative transfer, we will also consider additional feedback mechanisms which are of relevant interest for cosmological structure formation, namely, SN feedback and wind feedback. This represents a step further with respect to previous implementations, since they usually focus on individual feedback processes. We perform the implementation within the widely used and well-tested numerical N-body/SPH code GADGET (Springel 2005), in its most recent and updated version. In this way, we will be able to self-consistently study the effects of RT on chemical abundances, and to pinpoint the basic consequences for the cosmological evolution of the structures in the Universe.

In Sect. 2 we describe the implementations of radiation (Sect. 2.1) and cosmic chemistry evolution (Sect. 2.2). In Sect. 3, we test our implementation by performing analyses of the Strömgren sphere problem (Sect. 3.1) in a static (Sect. 3.1.1) and dynamic (Sect. 3.1.2) density field, and chemical abundance evolution (Sect. 3.2). We then apply our method to cosmological structure formation simulations (Sect. 4). We summarize, discuss and conclude in Sect. 5.

## 2 IMPLEMENTATIONS

We use the parallel tree N-body/SPH (smoothed particle hydrodynamics) code GADGET3, an extended version of the publicly available code GADGET2 (Springel 2005), and modify it in order to couple chemistry evolution and RT. In the following paragraphs, we give the details about the implementations of the RT (Sect. 2.1) and chemistry (Sect. 2.2) parts, and, in the next section, we will show results from our test runs.

### 2.1 Radiative transfer

To follow the propagation of radiation we use the implementation of RT in GADGET3 (Petkova & Springel 2009) and expand it to a multi-frequency scheme. The original implementation is based on a moment method, where the closure relation is the optically thin variable Eddington tensor, suggested by Gnedin & Abel (2001). To follow the transport of radiation, we solve the equation of anisotropic diffusion for the photon number density per frequency  $n_\gamma(\nu)$ :

$$\frac{\partial n_\gamma(\nu)}{\partial t} = c \frac{\partial}{\partial x_j} \left( \frac{1}{\kappa(\nu)} \frac{\partial n_\gamma(\nu) h^{ij}}{\partial x_i} \right) - c \kappa(\nu) n_\gamma(\nu) + s_\gamma(\nu), \quad (1)$$

where  $t$  is time,  $x_i$  and  $x_j$  are the coordinate components,  $c$  is the speed of light,  $\kappa(\nu)$  is the absorption coefficient,  $h^{ij}$  are the components of the Eddington tensor,  $s_\gamma(\nu)$  is the source function, and the Einstein summation convention is adopted for all exponents  $i$  and  $j$ .

The Eddington tensor is obtained by summing up the contributions from the sources of ionizing photons and its components are given by

$$h^{ij} = \frac{P^{ij}}{\text{Tr}(P^{ij})}, \quad (2)$$

where

$$P^{ij}(\mathbf{x}) = \int d^3x' \rho_*(\mathbf{x}') \frac{(\mathbf{x} - \mathbf{x}')_i (\mathbf{x} - \mathbf{x}')_j}{(\mathbf{x} - \mathbf{x}')^4} \quad (3)$$

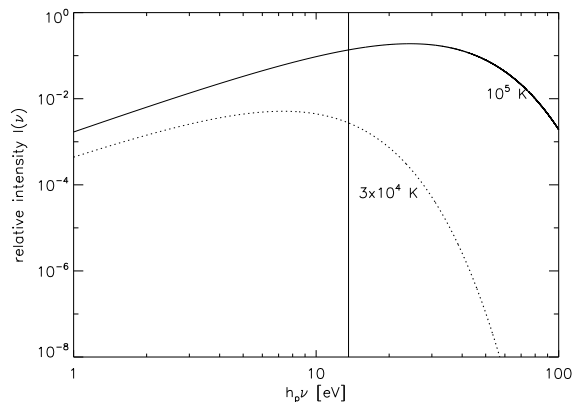


**Figure 1.** Intensity of a black-body spectrum as a function of photon energy in eV for two different effective temperatures -  $3 \times 10^4$  K and  $10^5$  K. The vertical line marks the end of the Lyman-Werner band at 13.6 eV.

is the radiation pressure tensor and  $\rho_*$  is the stellar density. The tensor is computed via a tree and effectively removes the dependence of the scheme on the number of ionizing sources – an advantage in cosmological and galaxy formation simulations.

The source term is treated in a *Strang-split* fashion, where photons are first “injected” into the medium surrounding the sources, and are then “diffused” via equation (1). Solving the equation for all particles in the simulation reduces to a linear system of equations, which we solve implicitly by using a Conjugate-Gradient scheme, that ensures robustness and stability even for large timesteps.

For our multi-frequency extension we need to transform the photon number density to ionizing intensity and vice versa. Since the photoheating and photoionization rates in equations (7) (discussed more in detail in Sect. 2.2) are obtained by integrating the intensity over frequency, we use a single photon number density in each frequency bin.

The photon number density per frequency is derived from the ionizing intensity,  $I(\nu)$ , as

$$n_\gamma(\nu) = \frac{1}{c} \frac{4\pi I(\nu)}{h_p \nu}, \quad (4)$$

where  $4\pi$  is the full solid angle and  $h_p$  is the Planck constant. For any particle and at any timestep, the RT equation (1) is then solved for each frequency bin.

The intensity of the radiative source,  $I(\nu)$ , depends on the particular problems treated. For stellar sources, a common, simple and suitable approximation (which we will also adopt in the following) is a black-body spectrum (see Fig. 1), with effective temperature dependent on the assumed stellar population. This treatment allows us to take into account contributions from a wide frequency range, even below the H-ionization energy of 13.6 eV. Indeed, as evident from the plot in Fig. 1 the low-energy tail of the black-body spectrum contributes to the Lyman-Werner band and that will definitely affect the molecular evolution of the gas (see later).

We note that dealing with radiation below  $\sim 13.6$  eV is a very debated and complicated problem (e.g. Thoul & Weinberg 1996; Haiman et al. 1997a,c; Omukai & Nishi 1999; Machacek et al. 2001; Kitayama et al. 2001; Ricotti et al.

**Table 1.** Ionization energies in [eV]

H	H <sup>-</sup>	He	He <sup>+</sup>	D	H <sub>2</sub>	HD	HeH <sup>+</sup>
13.6	0.7	24.6	54.4	14.9	15.4	15.4	44.5

2002a,b; Mackey et al. 2003; Shapiro et al. 2004; Dijkstra et al. 2004; Susa & Umemura 2004; Stacy et al. 2011), because of the many lines involved (76) in the LW band. Full, detailed modeling of RT in such regimes is beyond the aims of this work, and, at some levels, it might be superfluous (e.g. Ricotti et al. 2001), since the ionizing flux at high redshift ( $z$ ) is dominated by radiation from neighboring haloes (e.g. Ciardi et al. 2000), rather than from the soft-UV background in the LW band. Thus, H<sub>2</sub> photodissociation is simply accounted for by using (e.g. Abel et al. 1997; Ricotti et al. 2001; Yoshida et al. 2003; Ahn & Shapiro 2007; Maio et al. 2007; Whalen & Norman 2008) the radiative rate obtained from integration of the source intensity over the LW range, 11.2 – 13.6 eV – see eq. (7), in the next Sect. 2.2 – shielded according to Draine & Bertoldi (1996).

## 2.2 Chemistry

To couple radiation with chemistry, we include non-equilibrium reactions for H, He and molecule evolution (whose ionization and dissociation energies are quoted in Tab. 1), by following a chemical network (see Tab. 2) of several species: e<sup>-</sup>, H, H<sup>+</sup>, H<sup>-</sup>, He, He<sup>+</sup>, He<sup>++</sup>, H<sub>2</sub>, H<sub>2</sub><sup>+</sup>, D, D<sup>+</sup>, HD, HeH<sup>+</sup>. Besides some updates in the rates and in the reaction network, the implementation used is the same as the one in Maio et al. (2007) and Maio et al. (2010) (and based on Abel et al. 1997; Galli & Palla 1998; Yoshida et al. 2003). Since the main coolants at early times are H-derived molecules, H<sub>2</sub> (e.g. Saslaw & Zipoy 1967) and HD (e.g. Lepp & Shull 1984), the inclusion of a large network is crucial to correctly resolve the hydrodynamics and the fragmentation processes of high-redshift gas, as well demonstrated by e.g. Abel et al. (1997), Yoshida et al. (2003, 2006), Maio et al. (2006, 2007, 2009, 2010, 2011), Maio et al. (2011); Maio & Iannuzzi (2011).

To take into account chemical evolution, at each timestep and for each species  $i$ , the time variation of its number density  $n_i$  is computed, for collisional and photoionization/photodissociation events, via

$$\frac{dn_i}{dt} = \sum_p \sum_q k_{pq,i} n_p n_q - \sum_l k_{li} n_l n_i - k_{\gamma i} n_i, \quad (5)$$

where  $k_{pq,i}$  is the rate of creation of the species  $i$  from species  $p$  and  $q$ ,  $k_{li}$  is the destruction rate of the species  $i$  from collisions with species  $l$ , and  $k_{\gamma i}$  is the photoionization or photodissociation rate of species  $i$  due to radiation (see Tab. 1). The collisional rates are given by

$$k_{pq,i} = \int u \sigma_{pq,i}(u) f(u) d^3u, \quad (6)$$

(and the analogous for  $k_{li}$ ), with  $u$  relative velocity of particles  $p$  and  $q$ ,  $\sigma_{pq,i}(u)$  interaction cross-section, and  $f(u)$  Maxwellian velocity distribution function. More precisely, we do not compute the integrals on the fly, but instead we

interpolate pre-computed tables (whose references are listed in Tab. 2) in order to speed-up the code. These rates are temperature dependent and are expressed in units of volume per time, i.e. [cm<sup>3</sup> s<sup>-1</sup>] in the cgs system. As in the left-hand side, the first and second term in the right-hand side of equation (5) have dimensions of a number density per unit time, [cm<sup>-3</sup> s<sup>-1</sup>] in the cgs system.

Consistently with Sect. 2.1, when the species  $i$  interacts with radiation ( $\gamma$ ) – see Table 2 – and gets photo-ionized (like for H, D, H<sup>-</sup>, He, He<sup>+</sup>) or photo-dissociated (like for H<sub>2</sub>, H<sub>2</sub><sup>+</sup>, HD, HeH<sup>+</sup>), the corresponding radiative rate  $k_{\gamma i}$  can be written as

$$k_{\gamma i} = \int \frac{4\pi I(\nu)}{h_p \nu} \sigma_{\gamma i}(\nu) d\nu = \int c \sigma_{\gamma i}(\nu) n_{\gamma}(\nu) d\nu, \quad (7)$$

where the  $4\pi$  stands for isotropic radiation,  $I(\nu)$  is the source intensity as a function of frequency  $\nu$ ,  $\sigma_{\gamma i}(\nu)$  is the cross-section for the given process,  $h_p$  is the Planck constant,  $c$  the speed of light, and  $n_{\gamma}(\nu)$  the photon number density per frequency. In the final equality we made use of eq. (4), to formally get the rate expression similar to eq. (6). The radiative rates are probabilities per unit time, and are given in [s<sup>-1</sup>] in the cgs system. So, the number of radiative interactions per unit time and volume between photons and  $n_i$  particles is  $k_{\gamma i} n_i$ . The latter quantity is added on the right-hand side of equation (5) when photon interactions are taken in consideration, and consistently with the other terms in the equation, this is also given in units of number density per time, i.e. [cm<sup>-3</sup> s<sup>-1</sup>] in the cgs system.

When talking about radiative interactions, one has to consider that, while ionization energies (see Tab. 1) are uniquely defined, molecular dissociation energies might depend on the particular radiative process considered, and thus all the various channels must be taken into account. For example (see Tab. 2), LW radiation above the energy threshold of 11.2 eV can dissociate H<sub>2</sub> in 2H, but harder photons with energies larger than 15.42 eV would simply ionize the residual H<sub>2</sub> into H<sub>2</sub><sup>+</sup> + e<sup>-</sup>. Also for H<sub>2</sub><sup>+</sup> there are two possible branches: one above an energy threshold of 2.65 eV and below 21 eV (H<sub>2</sub><sup>+</sup> +  $\gamma$  → H<sup>+</sup> + H), and a second one between 30 eV and 70 eV (H<sub>2</sub><sup>+</sup> +  $\gamma$  → 2H<sup>+</sup> + e<sup>-</sup>). For the HeH<sup>+</sup> radiative interaction considered in our network the energy threshold is about 1.7 eV.

The set of differential equation (5) is integrated via simple linearization, so, given the timestep  $\Delta t$ , at each time  $t$  the temporal variation of the number fraction of species  $i$  can be written as

$$\frac{n_i^{t+\Delta t} - n_i^t}{\Delta t} = C_i^{t+\Delta t} - D_i^{t+\Delta t} n_i^{t+\Delta t}, \quad (8)$$

where we have introduced the creation coefficient for the species  $i$

$$C_i = \sum_p \sum_q k_{pq,i} n_p n_q, \quad (9)$$

in [cm<sup>-3</sup> s<sup>-1</sup>], and the destruction coefficient

$$D_i = \sum_l k_{li} n_l + k_{\gamma i}, \quad (10)$$

in [s<sup>-1</sup>]. The contribution from photoionization or photodis-

sociation is accounted for by adding, in equation (10), the  $k_{\gamma i}$  rates. The number density is updated from equation (8):

$$n_i^{t+\Delta t} = \frac{C_i^{t+\Delta t} \Delta t + n_i^t}{1 + D_i^{t+\Delta t} \Delta t}. \quad (11)$$

We apply this treatment to all the chemical species included, with the coefficients for each reaction in the network quoted in Table 2. Gas cooling or heating is computed from H and He collisional excitations (Black 1981; Cen 1992), ionizations (Abel et al. 1997), recombinations (Hui & Gnedin 1997b), H<sub>2</sub> and H<sub>2</sub><sup>+</sup> emissions (Galli & Palla 1998), HD emissions (Lipovka et al. 2005), Compton effect, and Bremsstrahlung (Black 1981).

The timestepping is limited by the cooling time,

$$t_{cool} = \left| \frac{E}{\dot{E}} \right|, \quad (12)$$

and by the electron recombination time,

$$t_e = \left| \frac{n_e}{\dot{n}_e} \right|, \quad (13)$$

where  $E$  and  $n_e$  are the energy and the electron number fraction of each particle, and  $\dot{E}$  and  $\dot{n}_e$  the corresponding time variations. For accuracy reasons in the abundance determinations, the chemical subcycles are done over 1/10 of  $\min(t_{cool}, t_e)$  (as described by e.g. Anninos et al. 1997; Abel et al. 1997; Yoshida et al. 2003; Maio et al. 2007). The additional constrain given by  $t_e$  is useful mostly when  $n_e$  changes very steeply, like behind the shock fronts, or at  $\sim 10^4$  K, below which hydrogen recombines very efficiently and above which hydrogen gets ionized very fast. Further details can be found in Maio et al. (2007) and references therein.

### 3 TEST SIMULATIONS

In order to test the implementation we perform numerical simulations under different conditions. First, we numerically solve an expanding ionized sphere problem (Sect. 3.1) by fully including both the RT and chemistry treatments. Then we show the cosmic evolution of the different chemical species, coupled with the radiative gas emissions (Sect. 3.2). Finally, we will perform cosmological simulations of early structure formation (Sect. 4) to check the effects of radiative feedback on gas cooling and collapse.

For all simulations we use a set of 284 frequencies, covering the range from 0.7 eV to 100 eV. The density of frequency bins around the peaks of the photoionization and photodissociation cross-sections is increased - i.e. there are more frequency bins in the spectral regions of interest. In this way we can ensure that photons are both traced and absorbed properly and no spectrum-averaging mistakes are made.

#### 3.1 Ionized sphere expansion

##### 3.1.1 Ionized sphere expansion in a static density field

The expansion of an ionization front in a static, homogeneous and isothermal gas is the only problem in radiation hydrodynamics that has a known analytical solution and is therefore the most widely used test for RT codes (e.g.

**Table 2.** Reaction network

Reactions	References for the rate coefficients
H + e <sup>-</sup> → H <sup>+</sup> + 2e <sup>-</sup>	A97 / Y06 / M07
H <sup>+</sup> + e <sup>-</sup> → H + γ	A97 / Y06 / M07
H + γ → H <sup>+</sup> + e <sup>-</sup>	A97 / Y06 / M07
He + e <sup>-</sup> → He <sup>+</sup> + 2e <sup>-</sup>	A97 / Y06 / M07
He <sup>+</sup> + e <sup>-</sup> → He + γ	A97 / Y06 / M07
He + γ → He <sup>+</sup> + e <sup>-</sup>	A97 / Y06 / M07
He <sup>+</sup> + e <sup>-</sup> → He <sup>++</sup> + 2e <sup>-</sup>	A97 / Y06 / M07
He <sup>++</sup> + e <sup>-</sup> → He <sup>+</sup> + γ	A97 / Y06 / M07
He <sup>+</sup> + γ → He <sup>++</sup> + e <sup>-</sup>	A97 / Y06 / M07
H + e <sup>-</sup> → H <sup>-</sup> + γ	GP98 / Y06 / M07
H <sup>-</sup> + γ → H + e <sup>-</sup>	A97 / Y06 / M07
H <sup>-</sup> + H → H <sub>2</sub> + e <sup>-</sup>	GP98 / Y06 / M07
H + H <sup>+</sup> → H <sub>2</sub> <sup>+</sup> + γ	GP98 / Y06 / M07
H <sub>2</sub> <sup>+</sup> + γ → 2 H <sup>+</sup> + e <sup>-</sup>	A97 / Y06 / M07
H <sub>2</sub> <sup>+</sup> + γ → H + H <sup>+</sup>	A97 / Y06 / M07
H <sub>2</sub> <sup>+</sup> + H → H <sub>2</sub> + H <sup>+</sup>	A97 / Y06 / M07
H <sub>2</sub> + H → 3H	A97 / M07
H <sub>2</sub> + H <sup>+</sup> → H <sub>2</sub> <sup>+</sup> + H	S04 / Y06 / M07
H <sub>2</sub> + e <sup>-</sup> → 2H + e <sup>-</sup>	ST99 / GB03 / Y06 / M07
H <sup>-</sup> + e <sup>-</sup> → H + 2e <sup>-</sup>	A97 / Y06 / M07
H <sup>-</sup> + H → 2H + e <sup>-</sup>	A97 / Y06 / M07
H <sup>-</sup> + H <sup>+</sup> → 2H	P71 / GP98 / Y06 / M07
H <sup>-</sup> + H <sup>+</sup> → H <sub>2</sub> <sup>+</sup> + e <sup>-</sup>	SK87 / Y06 / M07
H <sub>2</sub> <sup>+</sup> + e <sup>-</sup> → 2H	GP98 / Y06 / M07
H <sub>2</sub> <sup>+</sup> + H <sup>-</sup> → H + H <sub>2</sub>	A97 / GP98 / Y06 / M07
H <sub>2</sub> + γ → H <sub>2</sub> <sup>+</sup> + e <sup>-</sup>	A97 / Y06 / M07
H <sub>2</sub> + γ → 2 H	A97 / R01 / Y03 / M07
D + H <sub>2</sub> → HD + H	WS02 / M07
D <sup>+</sup> + H <sub>2</sub> → HD + H <sup>+</sup>	WS02 / M07
HD + H → D + H <sub>2</sub>	SLP98 / M07
HD + H <sup>+</sup> → D <sup>+</sup> + H <sub>2</sub>	SLP98 / M07
H <sup>+</sup> + D → H + D <sup>+</sup>	S02 / M07
H + D <sup>+</sup> → H <sup>+</sup> + D	S02 / M07
D <sup>+</sup> + e <sup>-</sup> → D + γ	GP98
D + γ → D <sup>+</sup> + e <sup>-</sup>	GP98
He + H <sup>+</sup> → HeH <sup>+</sup> + γ	RD82 / GP98 / M07
HeH <sup>+</sup> + H → He + H <sub>2</sub> <sup>+</sup>	KAH79 / GP98 / M07
HeH <sup>+</sup> + γ → He + H <sup>+</sup>	RD82 / GP98 / M07

Notes: γ stands for photons; P71 = Peterson et al. (1971); KAH79 = Karpas et al. (1979); RD82 = Roberge & Dalgarno (1982); SK87 = Shapiro & Kang (1987b); A97 = Abel et al. (1997); GP98 = Galli & Palla (1998); SLP98 = Stancil et al. (1998); ST99 = Stibbe & Tennyson (1999); R01 = Ricotti et al. (2001); WS02 = Wang & Stancil (2002); S02 = Savin (2002); GB03 = Glover & Brand (2003); Y03 = Yoshida et al. (2003); S04 = Savin et al. (2004); Y06 = Yoshida et al. (2006); M07 = Maio et al. (2007).

Iliev et al. 2006, 2009). For such a set-up, the ionized bubble around the ionizing source reaches a final steady radius, called the Strömgren radius, where absorptions and recombinations are balanced along the line of sight. For an H-only gas, the Strömgren radius is analytically given by

$$r_s = \left( \frac{3\dot{N}_\gamma}{4\pi\alpha_B n_H^2} \right)^{1/3}, \quad (14)$$

with  $\dot{N}_\gamma$  – the luminosity of the source in photons per second;  $\alpha_B$  – the case-B recombination coefficient; and  $n_H$  – the hydrogen number density. The case-B recombination co-

efficient assumes the so called 'on-the-spot' approximation, where photons from recombinations to lower energy levels are immediately absorbed in the vicinity of their emission (e.g. Spitzer 1978). If we approximate the ionization front (I-front) as infinitely thin, i.e. it features a discontinuity in the ionization fraction, the temporal expansion of the Strömgen radius can be solved analytically in closed form, with the I-front radius  $r_I$  given by

$$r_I = r_S [1 - \exp(-t/t_{\text{rec}})]^{1/3}, \quad (15)$$

where

$$t_{\text{rec}} = \frac{1}{n_H \alpha_B} \quad (16)$$

is the recombination time.

In our first test we perform an ionized sphere expansion, but we allow the temperature of the gas to vary in order to test the coupling between the RT and the full non-equilibrium chemistry treatment. As a reference, we compare to the analytical case with constant temperature. We follow the expansion of an ionized sphere around a source that emits  $\dot{N}_\gamma = 5 \times 10^{48}$  photons  $\text{s}^{-1}$ . The shape of the source spectrum corresponds to a  $3 \times 10^4$  K black body. The surrounding gas density is  $\rho = 1.7 \times 10^{-27}$  g  $\text{cm}^{-3}$  ( $\sim 10^{-3}$   $\text{cm}^{-3}$ ) and is sampled by  $16^3$ ,  $32^3$ , and  $64^3$  gas particles<sup>1</sup>. In the  $32^3$  case also the shielding of Draine & Bertoldi (1996) has been adopted, with the values cited in their paper. The initial temperature of the gas is set to  $T = 10^2$  K and is subject to photoheating and radiative cooling. At a temperature of  $10^4$  K, the case-B recombination coefficient is  $\alpha_B = 2.59 \times 10^{-13}$   $\text{cm}^3 \text{s}^{-1}$  (e.g. Iliev et al. 2009). Given these parameters, the recombination time is  $t_{\text{rec}} = 125.127$  Myr, and the expected Strömgen radius in the isothermal case (assuming  $T = 10^4$  K) is  $r_S = 5.4$  kpc. In Fig. 2, we show the evolution of the radial position of the I-front with time for the different resolutions. As a proxy for the position of the front we take the radius where the neutral and ionized hydrogen fractions are equal (see also Fig. 3).

All resolutions agree very well with each other. There is no difference in the case with shielding since the simulation never reaches the densities required to produce some effect, as discussed in the introduction. Our results agree within 10% with the analytical ones from equation (15). In particular, the simple analytical solution is systematically larger than the full-simulation trend, which is expected. This can be explained by the missing cooling contributions in the analytical calculations from, e.g., He,  $\text{H}_2$ ,  $\text{H}_2^+$ , HD that lower temperatures, enhance recombination, and make the Strömgen radius decrease (as visible in the simulated case). In fact, equation (15) is computed by assuming constant temperature for hydrogen-only gas (see also Petkova & Springel 2009), while, in the numerical calculations the full chemistry treatment of Table 2, including cooling and heating, is considered. Pawlik & Schaye (2011) find similar results in their one-dimensional ionized sphere simulations<sup>2</sup>.

<sup>1</sup> For more resolution studies, see Petkova & Springel (2009). There, it is shown that numerical convergence is reached already with  $8^3$  particles.

<sup>2</sup> Note that Pawlik & Schaye (2011) adopt a black body spectrum with effective temperature of  $10^5$  K and therefore produce different temperature and He radial profiles.

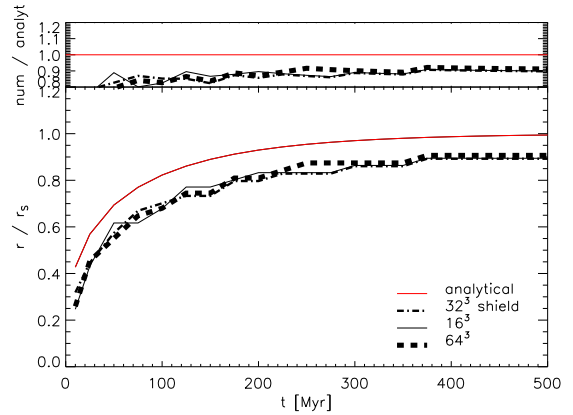


**Figure 2.** Evolution of the radial position of the I-front. The red line shows the analytic solution for an isothermal hydrogen only sphere. The black lines show our results from the simulations, assuming the radius is at the position where the amount of neutral and ionized hydrogen is equal. The thick dashed line shows the results from the simulation with  $64^3$  particles, the thinner dash-dotted line –  $16^3$  particles, and the thin solid line –  $32^3$  particles, where also  $\text{H}_2$  shielding has been adopted. All lines agree very well with each other, where the lowest resolution exhibits more scatter. The results from the simulation with shielding show that it can be discarded in set-ups like this, where no high particle number densities are reached. As shown in other studies (see text), the radius of the I-front stays always below the analytical solution given by eqn. 15.

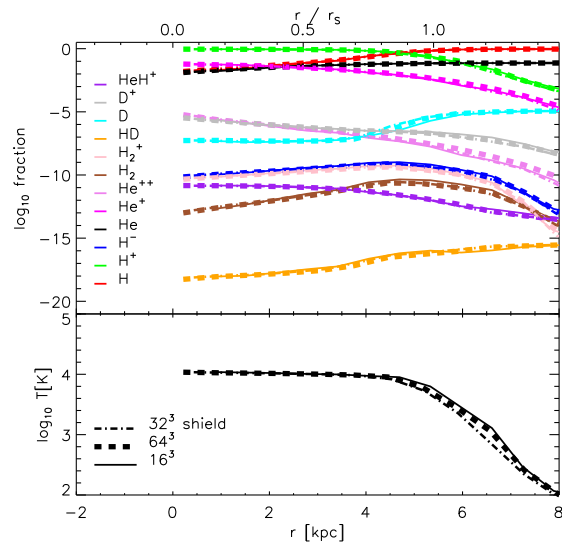
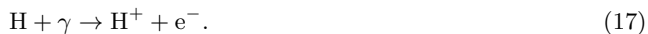


**Figure 3.** *Top panel:* Chemical abundance fractions radial profiles at 500 Myr after the source has been switched on. *Bottom panel:* Temperature radial profiles at 500 Myr after the source has been switched on. The temperature inside the ionized region reaches  $\sim 10^4$  K and extends beyond 6 kpc since harder photons, unabsorbed by the gas, heat the medium ahead of the ionization front. All simulations with different resolution and shielding agree very well with each other at all radii.

In Fig. 3, we show the radial profile of the temperature of the gas at 500 Myr after the source has been switched on. The temperature inside the ionized region reaches  $\sim 10^4$  K, consistently with photoheating from a stellar-type source, and extends beyond 5 kpc. Even further the temperature begins to drop. Harder photons (with energies  $> 60$  eV), that do not ionize the elements effectively, heat the medium ahead of the ionization front. If the source had a harder spectrum, e.g.  $10^5$  K black body, than the gas would be heated even at larger radii. We stress that at a distance of  $\gtrsim 5$  kpc (namely, around the Strömgren radius) temperatures steeply drop from  $\sim 10^4$  K down to  $\sim 10^3$  K and recombination processes take place (see next).

Correspondingly to the temperature profile, in Fig. 3, we display the radial profiles of the different chemical abundances at 500 Myr after the radiative source has been switched on. We assumed initial cosmic abundances<sup>3</sup>, which means that hydrogen species account for  $\sim 93\%$  of the total number densities and helium species for  $\sim 7\%$ . As expected, ionized fractions usually have larger values closer to the sources (within a few kpc), while neutral or molecular fractions increase at larger distances (above 3 – 6 kpc). In the following we discuss these trends, by referring to the reaction network of Table 2, in a more precise and detailed way.

• **Atomic hydrogen species:** due to the strong radiation intensities near the central source, hydrogen is kept completely ionized (i.e. the total hydrogen fraction,  $\sim 0.93$ , is in the ionized state,  $H^+$ ) within  $r \lesssim 5$  kpc by the dominant photoionization process



Only at larger radii, where the radiation intensity decreases, the recombination process



takes over and makes the  $H^+$  fraction drop down of several orders of magnitude, with the consequent increase of H fraction up to  $\sim 0.93$  (namely, the total hydrogen fraction is now in the neutral state).

$H^-$  is a very important species because it represents one of the main channels by which molecular hydrogen can be formed (see discussion later). It shows fractional values of  $\sim 10^{-9} - 10^{-10}$  until  $r \lesssim 6$  kpc and at larger distances drops of roughly 3 – 4 orders of magnitude. The increment of  $H^-$  fraction up to  $\sim 10^{-9}$  in correspondence of  $r \sim 4 - 5$  kpc is due to the simultaneous hydrogen recombination – eq. (18) – which leads to an increase of the neutral hydrogen and enhances the  $H^-$  formation via



reaction. In the innermost regions, due to the low ionization energy of only 0.755 eV,  $H^-$  photoionization



<sup>3</sup> They are set to:  $x_{e^-} \simeq 4 \times 10^{-4}$ ,  $x_H = 0.926$ ,  $x_{H^+} \simeq 4 \times 10^{-4}$ ,  $x_{H^-} = 10^{-19}$ ,  $x_{He} = 0.07$ ,  $x_{He^+} = 10^{-25}$ ,  $x_{He^{++}} = 10^{-30}$ ,  $x_{H_2} = 10^{-13}$ ,  $x_{H_2^+} = 10^{-18}$ ,  $x_{HD} = 10^{-16}$ ,  $x_D = 10^{-5}$ ,  $x_{D^+} = 10^{-7}$ ,  $x_{HeH^+} = 10^{-21}$ .

and collisional destruction by the abundant  $H^+$  and  $e^-$  species



determine a lower fraction of  $\sim 10^{-10}$ . At larger distances ( $r \sim 5 - 10$  kpc), H is dominant, but, contrary to reaction (19), free  $e^-$  are lacking and the most effective reactions are



that lead to a decrease of  $H^-$  fraction down to  $\lesssim 10^{-13}$ .

We note that a calculation of the exact analytical expression for the the Strömgren radius and a comparison with our results is not meaningful, since the analytical study is based on the simplified case of hydrogen-only gas and does not take into account interaction with other species and the effects of photoheating. However, the radius of the ionized hydrogen reaches  $\sim 5$  kpc, which is approximate to the expectation value of the Strömgren radius for the isothermal case.

• **Atomic helium species:** in the same way, due to the reactions



neutral He is efficiently destroyed at  $r \lesssim 3$  kpc, and the residual fraction is  $\sim 0.01$ .  $He^+$  and  $He^{++}$  reach fractions of  $\sim 0.06$  and  $\sim 10^{-5}$ , respectively, via



Moreover, the additional He depletion by  $H^+$  collisions leads to the formation of  $HeH^+$  (as we will discuss later). At  $r > 3$  kpc, the decreasing intensity of ionizing radiation – which plays the most relevant role in equations (26) and (29) – and the ongoing recombination processes which take away free electrons from the medium – needed e.g. in reactions (27), (28) – cannot sustain ionization any longer and the trends exhibit monotonic radial drops for both  $He^+$  and  $He^{++}$ . More exactly,  $He^+$  and He recombine according to



respectively, so, the final states of  $He^+$  and  $He^{++}$  are strictly linked to each other with abundances of  $\sim 10^{-5}$  and  $10^{-11}$  at  $r \sim 8$  kpc. Radiative interactions are weaker and weaker and they become practically negligible at large radii.

• **Atomic deuterium species:** the behaviour of D and  $D^+$  are quite regular and similar to H and  $H^+$ , with  $D^+$  being dominant at  $r \lesssim 5$  kpc and D dominant at  $r > 5$  kpc of  $\sim 3$  orders of magnitude. The abundances of deuterium and hydrogen species are bound by the balance reactions



but the most efficient processes are still photoionization ('close' to the source)



and recombination ('far' from the source)

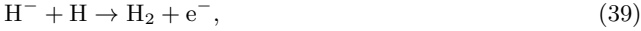


Minor contributions of D and D<sup>+</sup> are also involved for molecular species (see next) and can slightly affect H or H<sup>+</sup> production.

• **Molecular species:** Finally, we discuss the trends of molecular species (H<sub>2</sub>, H<sub>2</sub><sup>+</sup>, HD, HeH<sup>+</sup>). Their profiles are less regular and intuitive than atomic profiles, since more processes need to be addressed at the same time. For example, H<sub>2</sub> and H<sub>2</sub><sup>+</sup> have fractional values of  $\sim 10^{-13}$  and  $\sim 10^{-10}$ , respectively, at  $r \sim 1$  kpc, then, they show an increasing trend and a peak of  $\sim 10^{-10} - 10^{-9}$  at  $r \sim 4 - 6$  kpc. For larger  $r$ , they exhibit a drop off below  $\sim 10^{-14}$ , with H<sub>2</sub> overcoming H<sub>2</sub><sup>+</sup> at  $r > 7$  kpc. These behaviours are understood by considering that in the innermost regions the radiative negative feedback on molecule formation decreases for increasing  $r$ : this means that at larger radii radiation is not strong enough to dissociate molecules via



and, thanks to the available H, H<sup>+</sup> and e<sup>-</sup> (simultaneously present at  $r \sim 4 - 6$  kpc, where H recombination is still taking place), H<sub>2</sub> formation can proceed through the H<sup>-</sup> channel – see also reaction (19),



and through the H<sub>2</sub><sup>+</sup> channel,



This is the intrinsic reason why molecular hydrogen roughly follows the H<sup>-</sup> profile discussed earlier. Obviously, residual photons will slightly boost the ionized fraction of H<sub>2</sub><sup>+</sup> (with respect to H<sub>2</sub>) via



until  $r \sim 7$  kpc. At larger distances, photons are too weak to ionize the gas, so H<sub>2</sub> takes over and H<sub>2</sub><sup>+</sup> drops dramatically of  $\sim 3$  orders of magnitude within 1 kpc. Additionally, we note that the sharp decrement of molecular fractions at very large distances is basically due to the fact that the medium becomes almost completely neutral and the ionized fractions of e<sup>-</sup> and H<sup>+</sup> are too low to boost H<sup>-</sup> and H<sub>2</sub><sup>+</sup>, and, hence, H<sub>2</sub> formation.

Similarly, the increase with radius of HD fraction is essentially caused by the weakening of the central radiation and of H<sup>+</sup> and e<sup>-</sup> fractions which are less and less effective in dissociating it at larger  $r$ . In particular, at  $r \lesssim 4$  kpc, H, D and H<sub>2</sub> are subdominant with respect to their ionized counterparts H<sup>+</sup>, D<sup>+</sup> and H<sub>2</sub><sup>+</sup>, thus, HD formation due to



is strongly inhibited, while little contributions come from



Destruction from reaction



further lower HD abundances around  $\sim 10^{-18}$  level. At  $r \gtrsim 4$  kpc, hydrogen and deuterium recombinations, together with H<sub>2</sub> formation via H<sup>-</sup> channel, support HD formation through reactions (43) and (44), instead reaction (45) is no longer effective. As a consequence, the HD fractional abundance grows more than  $\sim 2$  orders of magnitude at  $r \sim 8$  kpc.

We note that a boost of HD production in shock-compressed gas was expected because of the simultaneous increment of H<sub>2</sub> fractions, quite visible in Fig. 3, in correspondence of the Strömgreen radius.

For what concerns the aforementioned HeH<sup>+</sup>, this is efficiently produced near the source because there are a lot of free protons which can boost its abundance via



even in a more powerful way than photodissociation



Only when protons are lacking (i.e. at large  $r$ ) HeH<sup>+</sup> production is inhibited up to  $\sim 3$  orders of magnitude and drops from  $\sim 10^{-11}$  to  $\sim 10^{-14}$ .

We stress that the residual relative ionized fractions far from the source ( $r \sim 8$  kpc) are:  $n_{\text{H}^+}/n_{\text{H}} \sim 10^{-3}$ ,  $n_{\text{D}^+}/n_{\text{D}} \sim 10^{-3}$ ,  $n_{\text{H}^-}/n_{\text{H}} \sim 10^{-13}$ ,  $n_{\text{He}^+}/n_{\text{He}} \sim 10^{-3}$ ,  $n_{\text{He}^{++}}/n_{\text{He}} \sim 10^{-9}$ ,  $n_{\text{H}_2^+}/n_{\text{H}_2} \sim 10^{-1}$ . The absolute values quoted in the previous discussion are dependent on the initial composition assumed for the gas. Although the qualitative behaviour is not supposed to change much, larger or smaller values for the assumed fractions could result in more efficient or less efficient formation and destruction processes. However, the general trends are supposed to be quite independent from that.

The test presented here is based on the initial conditions of Iliev et al. (2009), but different works are available in literature. Results that are going in the same direction were in fact found by e.g. Ricotti et al. (2001); Ahn & Shapiro (2007); Whalen & Norman (2008), who developed, independently, different H, He, and H<sub>2</sub> chemistry networks. Their simulation setups were very different, though, and the parameters for the central source, as well.

Ricotti et al. (2001) (their Fig. 3) performed the first one-dimensional calculations of a star shining in a primordial mini-halo. A popIII-like source with a power-law spectrum and  $\dot{N}_\gamma \simeq 1.2 \times 10^{49} \text{ s}^{-1}$  at  $z \simeq 19$  was located in a static, uniform medium at the mean density  $\bar{n}(z \simeq 19) \simeq 0.1 \text{ cm}^{-3}$ . They studied the behaviour of the molecular species after  $\sim 100$  Myr from the explosion of the central star, when the Strömgreen radius had reached  $\sim 4$  kpc, and a corresponding peak of H<sub>2</sub> with  $x_{\text{H}_2} \sim 5 \times 10^{-4}$ , a few kpc wide, had formed. This was equivalent to a boost of about 3 orders of magnitude with respect to their initial  $x_{\text{H}_2} \sim 10^{-6}$  value assumed. Also in our previous discussion, despite the different initial values, we have found an increase in the H<sub>2</sub> fraction of  $\sim 3$  orders of magnitude.

Similarly, Ahn & Shapiro (2007) (their Fig. 8) and Whalen & Norman (2008) (their Fig. 1) performed one- and three-



dimensional calculations, respectively, considering a  $120 M_{\odot}$  popIII-like source with a blackbody spectrum having effective temperature of  $T_{eff} = 10^5$  K and  $\dot{N}_{\gamma} \simeq 1.5 \times 10^{50} \text{ s}^{-1}$ . They assumed the star to be in a primordial halo with a truncated isothermal sphere density profile, whose central matter densities were reaching up  $\gtrsim 4 \times 10^{-22} \text{ g cm}^{-3}$ . They focused on the innermost core of the star forming regions, after roughly 0.6 times the lifetime of the massive popIII stars (a few Myr), when the Strömgreen radius was still around  $\lesssim 30$  pc and a corresponding peak of  $\text{H}_2 \sim 10$  pc wide had arisen. They also find an increase to  $x_{\text{H}_2} \sim 10^{-4}$ , a few orders of magnitude larger than the assumed initial value of  $x_{\text{H}_2} \sim 10^{-6}$ .

The first relevant difference with the study presented here is in the assumed  $\dot{N}_{\gamma}$  (our value is  $5 \times 10^{48} \text{ s}^{-1}$ ): Ricotti et al. (2001) used an  $\dot{N}_{\gamma}$  2.2 times larger, while Ahn & Shapiro (2007) and Whalen & Norman (2008) used a value 300 times larger. Consequently, the number of photons available to ionize atoms or dissociate molecules is much bigger in their cases, than in ours. This explains why they find  $\text{H}_2$  fractions more significantly destroyed in the inner regions. Then, molecule dissociation or creation is also strictly linked to the typical conditions of the medium. In the aforementioned works, this is denser than in ours (of  $\sim 2 - 4$  orders of magnitude), and have strong implications when computing abundances, since higher densities allow easier collisional dissociation in the inner, ionized regions. When temperatures fall below  $\sim 10^4$  K,  $\text{H}_2$  creation becomes more efficient and larger free-electron number densities can lead to a noticeable increase of molecular fractions<sup>4</sup>. This is actually the reason why the profiles of our low-density gas in Fig. 3 show  $\text{H}_2$  increases up to only  $\sim 10^{-10}$ , while very overdense gas can reach  $\text{H}_2$  fractions of  $\sim 10^{-4}$  in front of the propagating I-front.

We conclude by noticing that, despite the huge diversities in the parameters and in the  $\text{H}_2$  peak values, the different behaviours of the profiles are in qualitative agreement, showing an increment of the molecular fractions in correspondence of the I-front, and orders-of-magnitude declines farther away. Together with the  $\text{H}_2$  raise (within a shell of  $\sim 2$  kpc) the consequent HD increment is obviously expected to be more prominent in high-density environments.

None the less, the final effects on triggering star formation are not completely clear, since gas runaway collapse can be significantly enhanced only when densities are larger than  $\sim 1 - 10 \text{ cm}^{-3}$ , and molecular fractions increase up to  $> 10^{-2}$  (see further discussions in Sect. 4).

### 3.1.2 Ionized sphere expansion in a dynamic density field

In this section we repeat the test from the previous one, but we allow the gas particles to move due to pressure forces, but not gravity. The density field is not static anymore. The resolution we have chosen here is  $32^3$  gas particles.

The position of the I-front in this stage is given by (Spitzer 1978)

<sup>4</sup> For example, electron fractions of  $\sim 10^{-4}$  determine typical IGM fractions for  $\text{H}_2$  of  $\sim 10^{-6}$ , instead, in gas with overdensities of  $\sim 10^4$ ,  $\text{H}_2$  fractions can be boosted up to  $\sim 10^{-3}$  (Ahn & Shapiro 2007).

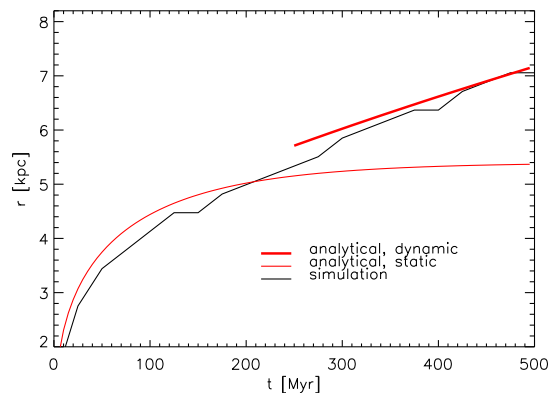


**Figure 4.** Evolution of the radial position of the I-front. The dashed line shows our results from the simulation, assuming the radius is at the position where the amount of neutral and ionized hydrogen is equal. The solid line is the result from eq. (15), computed by assuming isothermal gas at  $10^4$  K. The extension of the solid line is given by eq. (48). The results from the simulation agree very well with the analytical results, also at radii beyond the Strömgreen radius  $r_S$ .

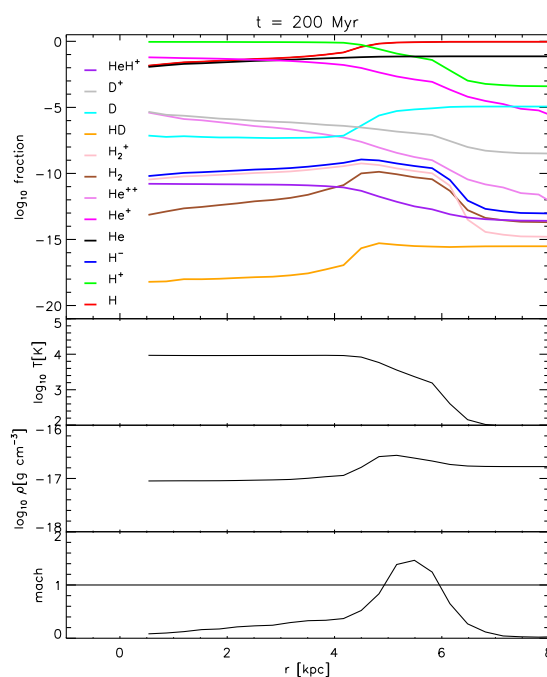


**Figure 5.** Top panel: Chemical abundance fractions radial profiles at 500 Myr after the source has been switched on. Bottom panel: Temperature, density, and Mach number radial profiles at 200 Myr after the source has been switched on. The temperature inside the ionized region reaches  $\sim 10^4$  K and extends beyond 6 kpc since harder photons, unabsorbed by the gas, heat the medium ahead of the ionization front. A shock, a  $\text{H}_2$  shell, and an HD boost have developed ahead of the I-front.

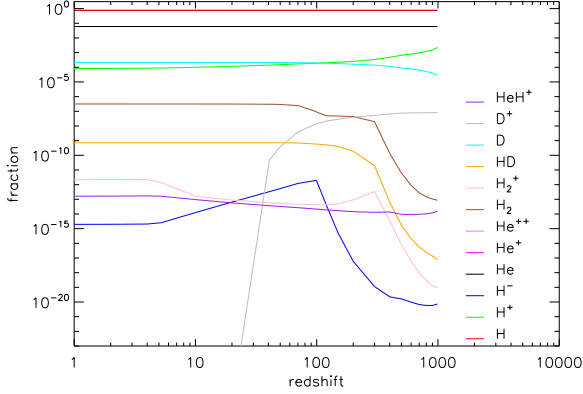


**Figure 6.** Number fraction evolution as a function of redshift for the different chemical species, followed in our implementation. The background cosmology is a standard flat  $\Lambda$ CDM model with geometrical parameters:  $\Omega_{0,\text{tot}} = 1.0$ ,  $\Omega_{0,\Lambda} = 0.7$ ,  $\Omega_{0,m} = 0.3$ ,  $\Omega_{0,b} = 0.04$ .

$$r_1 = r_S \left( 1 + \frac{7c_s t}{4r_S} \right), \quad (48)$$

where  $c_s$  is the sound speed of the ionized gas and  $r_S$  is the Strömngren radius given by equation (15).

In Fig.4 we show the evolution of the position of the I-front and its velocity with time. We compare with analytical results from equations (15) and (48). We note that the I-front follows the analytical prediction for static gas in the beginning of the expansion. After approximately 200 Myr at approximately 5 kpc from the source, the I-front continues to move outwards, rather than start to decelerate, and follows the dynamic gas solution given above.

In Fig. 5 we present the radial profiles of the different species, the temperature, and the density of the gas at  $t = 200$  Myr after the source has been switched on. The temperature in the ionized sphere is  $\sim 10^4$  K and there is a shock and a density contraction ahead of the I-front, which moves at super-sonic speed at this evolution time. We also note that there is a HD boost and a  $\text{H}_2$  shell ahead of the I-front as well, inside the density contraction region. Similar results have been shown also by Ricotti et al. (2001). These conditions – increased density and increased  $\text{H}_2$  fraction are favorable for star formation.

### 3.2 Cosmological abundance evolution

In order to test how our implementation performs during cosmological evolution, we run the chemical network coupled with the RT network for the mean background density evolution and follow the changes in the different species as a function of the cosmic time. The radiative source is assumed to be the uniform CMB radiation with a black body spectrum with effective temperature of  $\sim 2.73(1+z)$  K. The CMB radiation is self-consistently followed, according to the treatment outlined in Sect. 2. The initial fractions,  $x$ , for the different species<sup>5</sup> are initialized, at redshift  $z \simeq 10^3$ , accord-

ingly to a neutral plasma at  $\sim 10^3$  K (see e.g. Galli & Palla 1998).

We present the results in Fig. 6, where the cosmic mean number fractions as a function of redshift are plotted for a standard flat  $\Lambda$ CDM cosmology with geometrical parameters  $\Omega_{0,\text{tot}} = 1.0$ ,  $\Omega_{0,\Lambda} = 0.7$ ,  $\Omega_{0,m} = 0.3$ ,  $\Omega_{0,b} = 0.04$ . The H and He number fractions are unaffected by the redshift evolution.

At early times, some residual recombination process continue taking place, while the CMB temperature goes down, and make  $\text{H}^+$  evolution drop from a fraction of  $\sim 10^{-3}$ , at  $z \sim 1000$ , to the final  $\lesssim 10^{-4}$  value. The evolution of  $\text{H}^-$  clearly shows the effects of free electrons at high redshift that boost its formation (and H-derived molecule formation) from  $x_{\text{H}^-} \sim 10^{-20}$ , at  $z \sim 1000$ , to  $x_{\text{H}^-} \sim 10^{-12}$ , at  $z \sim 100$ . The following hydrogen recombination implies a decrease both in  $\text{H}^+$  and  $e^-$  fraction, with consequent drop of  $\text{H}^-$  (see Table 2) down to  $x_{\text{H}^-} \sim 10^{-15}$  at low redshift. The two ionization states of He are constantly kept at very low values, close to the initial ones (their trends are not displayed in Fig. 6 for sake of clarity).

As already mentioned, hydrogen molecule formation is initially enhanced due to the available residual  $e^-$  and the progressively diminishing effects of CMB radiation: this allows hydrogen to increasingly form  $\text{H}_2^+$ , with a peak around  $z \sim 300$ , and  $\text{H}_2$ , until  $z \sim 70$ .  $\text{H}_2^+$  formation is efficiently driven by H and the available  $\text{H}^+$  in primordial times. At  $z \lesssim 300$ , paucity of free protons (whose fraction in the meantime has dropped of about one order of magnitude) make difficult  $\text{H}_2^+$  formation. However, the continuous increment of  $\text{H}^-$  enhances  $\text{H}_2$  at  $z \sim 100$ , and afterward its formation is mainly driven by the  $\text{H}^-$  channel, rather than the  $\text{H}_2^+$  one, until  $z \sim 70$ . The dominant formation path at different times is clearly recognizable when comparing the  $\text{H}_2$  trend with the  $\text{H}_2^+$  and  $\text{H}^-$  trends. The  $z \sim 300$  peak of  $\text{H}_2^+$  corresponds to the steep increase of  $x_{\text{H}_2}$  at early times, while the  $z \sim 100$  peak of  $\text{H}^-$  corresponds to the following boost at later times. For  $z \lesssim 70$ ,  $x_{\text{H}_2}$  stays roughly constant between  $10^{-7} - 10^{-6}$  because further production is halted by the decrement of free protons and electrons, and radiative destruction cannot take place because of the low CMB flux at low redshift.

Deuterium is also affected by cosmological evolution and the weaker CMB intensity effects at lower redshift. Thus, recombination of D and  $\text{D}^+$  make  $x_{\text{D}}$  increase up to  $\sim 10^{-4}$  and  $x_{\text{D}^+}$  dramatically drop down at  $z < 100$ . The simultaneous ongoing  $\text{H}_2$  formation at  $z \gtrsim 70$  also ‘drags’ HD fractions up to  $\sim 10^{-9}$  levels (HD is very sensitive to  $\text{H}_2$  abundances).

The  $\text{HeH}^+$  molecule is often formed behind fast shocks (e.g. Neufeld & Dalgarno 1989) by He and  $\text{H}^+$ , but, due to its low dissociation energy (of  $\sim 14873.6 \text{ cm}^{-1} \simeq 1.7 \text{ eV}$ ; Bishop & Cheung 1979) it can be found and emitted only below  $\sim 10^4$  K. Moreover, the presence of background radiation can dissociate it in its two components soon after the recombination epoch, at  $z \lesssim 10^3$ . Indeed, the plot in Fig. 6 highlights how  $\text{HeH}^+$  is initially underabundant and then is gradually formed while the Universe expands, cools and the

<sup>5</sup> They are set to:  $x_{e^-} \simeq 4 \times 10^{-4}$ ,  $x_{\text{H}} = 0.926$ ,  $x_{\text{H}^+} \simeq 4 \times 10^{-4}$ ,  $x_{\text{H}^-} = 10^{-19}$ ,  $x_{\text{He}} = 0.07$ ,  $x_{\text{He}^+} = 10^{-25}$ ,  $x_{\text{He}^{++}} = 10^{-30}$ ,

$x_{\text{H}_2} = 10^{-13}$ ,  $x_{\text{H}_2^+} = 10^{-18}$ ,  $x_{\text{HD}} = 10^{-16}$ ,  $x_{\text{D}} = 10^{-5}$ ,  $x_{\text{D}^+} = 10^{-7}$ ,  $x_{\text{HeH}^+} = 10^{-21}$ .

CMB radiation gets weaker. Over the cosmic time  $x_{\text{HeH}^+}$  slightly increases of one order of magnitude, from  $\sim 10^{-14}$  up to  $\gtrsim 10^{-13}$ , and, due to H interactions, it sustains  $\text{H}_2^+$  with subsequent  $\text{H}_2$  formation.

The low radiation intensity of the CMB is not able to produce large changes in the abundances of the elements, but is never the less a good test on the performance of our implementation. Our results agree very well with previous cosmological abundance evolution studies as e.g. Abel et al. (1997); Galli & Palla (1998); Maio et al. (2007).

The presence of an additional cosmic UV radiation during reionization (e.g. Haardt & Madau 1996) at low redshift ( $z \lesssim 7$ ), would heat the medium and change the ionization equilibria. As a consequence, one might expect more free electrons, larger  $\text{H}_2^+$  and  $\text{H}^-$  abundances and hence more  $\text{H}_2$  production, accompanied by increased  $\text{D}^+$  and HD fractions, and dissociation of  $\text{HeH}^+$ .

#### 4 APPLICATION: COSMOLOGICAL STRUCTURE FORMATION

As a final application, we present results from a cosmological structure formation simulations in the framework of the standard  $\Lambda\text{CDM}$  model, and we will also consider additional feedback mechanisms from star formation (as already mentioned in Sec. 1). We use a periodical comoving boxsize of  $L_{\text{box}} = 0.5h^{-1}\text{Mpc}$  on a side with  $2 \times 64^3$  gas and dark-matter particles (for a resulting spacial resolution of  $\sim 0.4\text{kpc}/h$  comoving), sampled at the initial redshift  $z = 100$ . The runs include gravity, hydrodynamics, wind feedback, non-equilibrium chemistry, and radiative transfer. Stars are taken to be sources of ionizing radiation. Since each star particle in the simulation represents a whole stellar population with a Salpeter distribution, about 12% of its mass is in high-mass stars ( $\gtrsim 10M_{\odot}$ ) that are able to produce UV photons. The frequency distribution is assumed to be a black-body spectrum with an effective temperature of  $3 \times 10^4\text{K}$ , which corresponds to a luminosity of approximately  $8 \times 10^{48}\text{photons s}^{-1}$  per high-mass star in the stellar population of the star particle. We assume that gas particles are converted into stars once a critical density of  $\sim 10\text{cm}^{-3}$  is reached, and the gas temperature is below  $\sim 10^4\text{K}$  to make sure that the gas is effectively cooling (see details in Maio et al. 2009). Star forming particles also experience SN-explosion feedback, which heats the gas above  $\sim 10^5\text{K}$ , and wind feedback, which expels gas with a typical velocity of  $\sim 500\text{km/s}$  (see also Springel 2005, and references therein).

A pictorial representation of the simulated box is given in Fig. 7, where we show mass-weighted temperature slices through the simulation volume at redshift  $z = 10.61$  and  $z = 6.14$  for the full run, including, in particular, both non-equilibrium chemistry and RT.

The first sources are well visible close to the central part of the slice, and, while the structure growth proceeds, more sources are found in scattered places along the converging filaments. Obviously, in a wider perspective (say on  $\sim 100\text{Mpc}$  scale), radiative sources would be much more uniformly distributed. However, there are currently serious computational limitations for performing simulations with such large box sides and, simultaneously, with resolution good enough to resolve chemical evolution and radiative transfer at the same

time. In the maps, the filamentary cold structures led by early molecular gas are well visible at temperatures around hundreds Kelvin. In the densest regions, radiative effects from first stars heat the medium above  $\sim 10^4\text{K}$  already by redshift  $z \gtrsim 10$ . More and more star formation episodes appear at later stages and contribute to the cosmic reionization process down to redshift  $z \simeq 6$ .

Given the small size of our box, we can clearly focus on the infalling phases of the cold material in the intersection of primordial filamentary structures, and on the subsequent SN explosions, which heat the gas and push material into the lower-density, void regions. This helps understanding the different role played by the various feedback mechanisms, on the other side, the lack of a very large box also leads to an insufficient number of stellar sources to fully complete reionization by  $z \sim 6$ .

In Fig. 8 we plot the phase diagrams (gas temperature vs. number density) for the simulations with and without radiative treatment. The colors refer to the  $\text{H}_2$  mass fraction. Molecular hydrogen is dissociated in the presence of ionizing radiation (mostly in the Lyman-Werner band), and this effect increases with decreasing redshift, due to the higher number of available photons. As a consequence, this lowers the star formation process, since  $\text{H}_2$  provides the largest part of the sub- $10^4\text{K}$  cooling. It is evident from the plots that without radiative feedback  $\text{H}_2$  can reach levels  $\gtrsim 10^{-2}$  and boost early star formation. In presence of radiation from stellar sources, molecular fractions decrease of several orders of magnitude down to  $\lesssim 10^{-4}$ . This effect is stronger for low-density gas, where molecules re-form more slowly. Such behaviour is clear from the both cases shown, at redshift  $z = 10.61$  and  $z = 6.14$ . In the latter case, a wider temperature spread, due to thermal heating of the infalling gas at low density, appears as a consequence of the ongoing structure formation. Additionally, also SN-heated gas at  $10^5 - 10^6\text{K}$  is evident with extremely low molecular fractions ( $\lesssim 10^{-16}$ ). The lack of very cold gas in the more realistic case with both chemistry and RT suggests that low-temperature cooling by metals (e.g. Maio et al. 2007) could be an important mechanism to sustain star formation after the first generation of stars (Maio et al. 2010)<sup>6</sup>. To better underline the impacts of radiative effects on early chemistry, we also show in Fig. 9 the redshift evolution of the mean and maximum number fractions of the two main molecules,  $\text{H}_2$  and HD, and of the basic species for the different channels of molecular formation,  $\text{H}^-$  and  $\text{H}_2^+$ .

As mentioned previously, after early star formation sets in, around redshift  $z \sim 12$ , the  $\text{H}_2$  fractions drops by several orders of magnitude (from average values of  $\sim 10^{-5}$  down to  $\lesssim 10^{-10}$ ), as ionizing radiation starts to propagate in the simulated volume. This is not seen in the case without radiation, where  $\text{H}_2$  increases almost monotonically, with peak values of  $\sim 10^{-2}$  at  $z \simeq 6$ .

The mean HD fraction stays roughly constant in the presence of ionizing radiation, but it is increasing in the case without radiation. When comparing peak values, one sees that, at  $z \simeq 12$ , HD has fractions of  $\sim 10^{-6}$  in both cases, but in the RT case, it is significantly destroyed when

<sup>6</sup> One could also rely on reionized gas (Yoshida et al. 2007) to form subsequent baryonic structures.

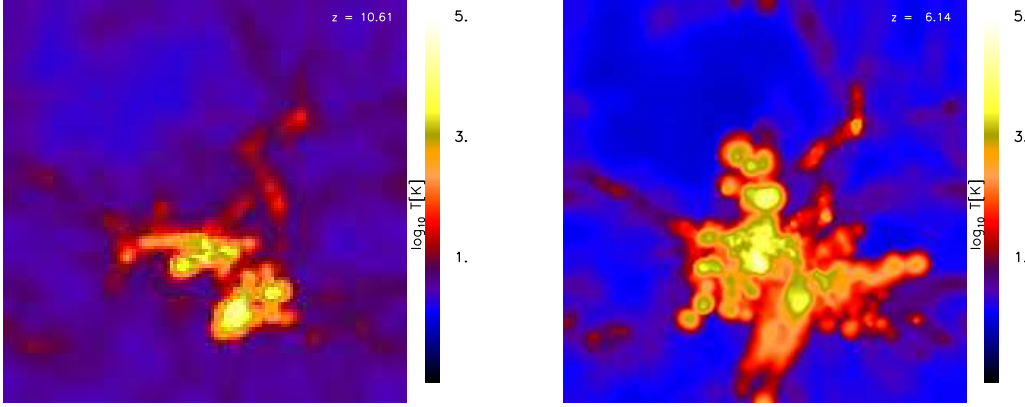


**Figure 7.** Mass-weighted temperature slices through the box at redshift  $z = 10.61$  (left) and  $z = 6.14$  (right). The simulation includes feedback effects, full non-equilibrium chemistry and RT (see text).

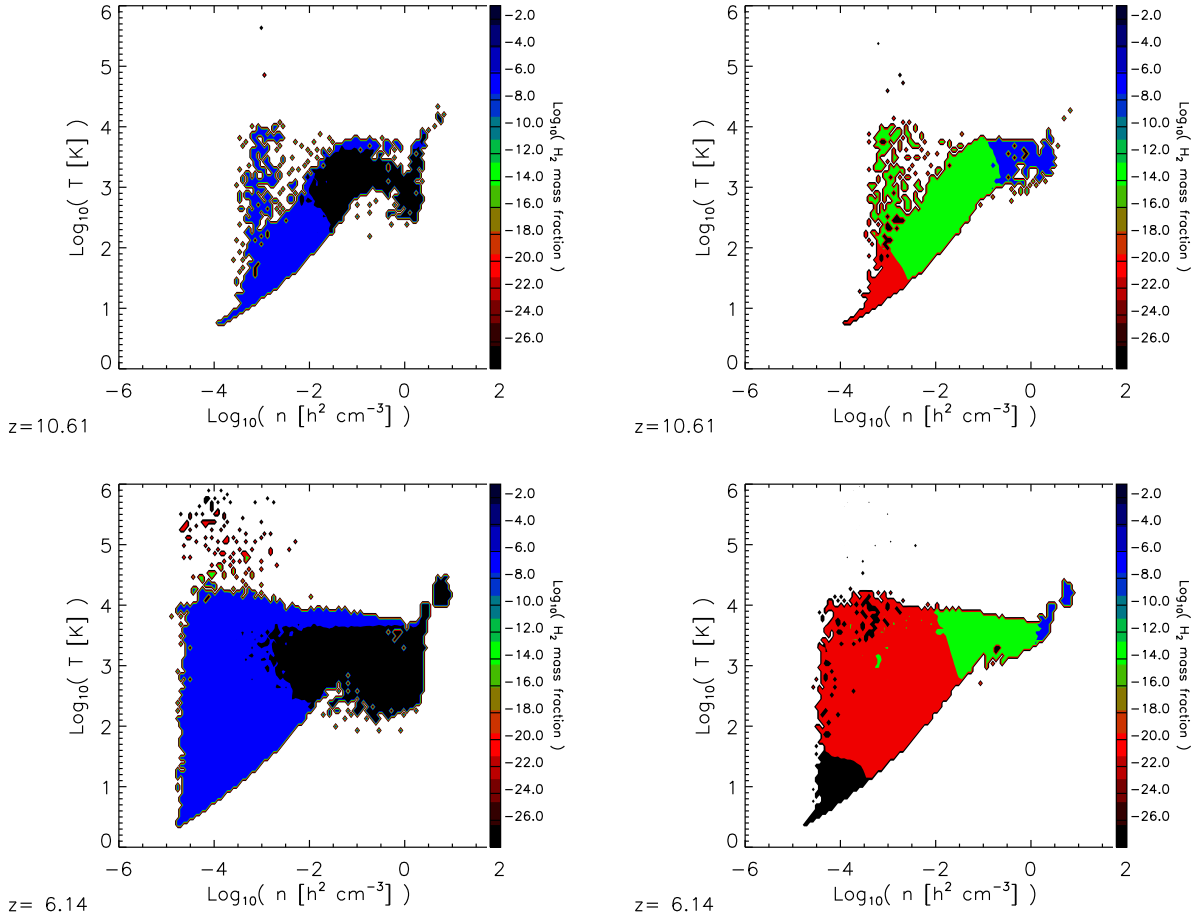


**Figure 8.** Phase diagrams - temperature versus gas comoving number density at redshift  $z \sim 10$  (top) and redshift  $z \sim 6$  (bottom) for a simulation without (left) and with (right) ionizing radiation. The color shows the mass fraction of  $\text{H}_2$ . In the presence of ionizing radiation,  $\text{H}_2$  is depleted on all scales by many orders of magnitude. The effect is stronger at lower redshift due to the larger number of photons available.

photons begin to propagate. Instead in the non-RT case its maximum values catch up with  $\text{H}_2$ .

The  $\text{H}^-$  fraction is crucial for  $\text{H}_2$  formation via the  $\text{H}^-$ -channel: in presence of RT its mean values are lowered down to  $\sim 10^{-12}$ , so they cannot catalyze efficiently further

molecule formation, while in the non-RT case,  $\text{H}^-$  would increase by two orders of magnitude.

Similarly,  $\text{H}_2^+$  catalyzes  $\text{H}_2$  formation via the  $\text{H}_2^+$ -channel, but photon propagation destroys molecules and inhibits  $\text{H}_2^+$  formation. As a comparison, in the non-RT run

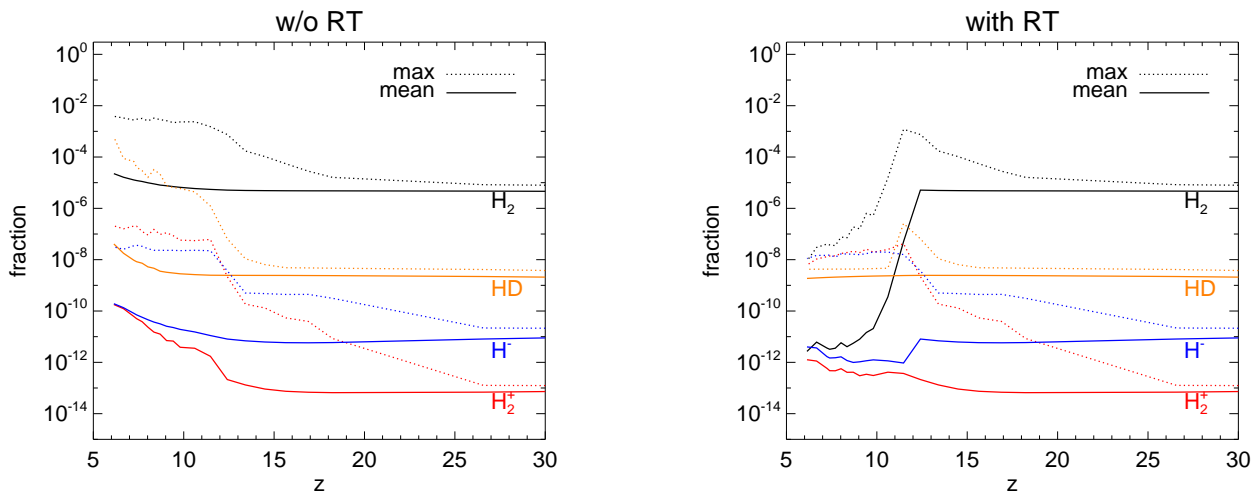


**Figure 9.** Evolution of the mean and maximum  $H_2$ , HD,  $H^-$  and  $H_2^+$  fractions with redshift for the simulation with ionizing radiation (right) and without (left). When star formation sets in at redshift  $z \sim 11$ , the  $H_2$  fractions drop fast, where both the mean and the maximum values are affected. The mean HD fraction stays constant in the presence of ionizing radiation and is increasing with lower redshift in the absence of radiation. The maximum follows the same trend, with the difference that it drops down as the first photos begin to propagate. There is only a small change in the evolution of the  $H^-$  fraction. Finally, the  $H_2^+$  fraction is slightly suppressed from the ionizing radiation.

$H_2^+$  reaches mean values of  $\sim 10^{-10}$ , a couple of orders of magnitude larger than in the RT run. Maximum fractions for  $H^-$  and  $H_2^+$  are similarly suppressed of about one order of magnitude.

As a conclusion, the radiative feedback is responsible for molecule dissociation. Molecules are easily depleted not only from the external sources, but also from the central sources which have just been formed. This is justified by the fact that catastrophic molecular cooling sets in already at densities  $\gtrsim 1 \text{ cm}^{-3}$ , when the material is optically thin, and thus there is no significant gas shielding preventing  $H_2$  and HD dissociation. In fact, in the simulations presented here, radiative feedback becomes effective at densities  $> 10 \text{ cm}^{-3}$ . In the innermost central regions (i.e. below a few hundreds of comoving parsec, not sampled by our simulations because of resolution limits), densities could rise up to values greater than  $\sim 10^8 \text{ cm}^{-3}$ , become optically thick, and produce significant shielding<sup>7</sup>. This should not affect the overall molecular destruction over  $\sim \text{kpc}$  scales by external sources, though.

We stress that precise, quantitative assessments about the net effects of radiative feedback on the surrounding gas are difficult, because one should be able to prove RT on very different scales within N-body/hydro chemistry calculations. While destruction of molecules in low-density intergalactic medium (IGM) is intuitive and expected, the behaviour in the innermost cores of collapsed objects is quite debated and strongly dependent on the local density regime. In particular, as pointed out by Susa (2007), the ignition timing of the source star is crucial in collapsing clouds: if the ig-

<sup>7</sup> If we consider that primordial haloes have radii of a few kpc, the fraction of volume interesting for such events is very small: for a protogalaxy having a radius of  $\sim \text{kpc}$  and developing a dense core within  $\sim 100 \text{ pc}$ , the volume fraction of high-density, possibly shielded gas is  $\lesssim 10^{-3}$ .

nitiation takes place when the central density is larger than  $\sim 10^3 - 10^4 \text{ cm}^{-3}$ , the collapse cannot be halted by radiation. However, in great detail the stellar-core formation and the ignition of nuclear reactions which lead the birth of the star is nowadays still prohibitive.

As a consequence, cosmological simulations are inevitably affected by resolution issues, mostly at large densities, that limit the possibility of fully understanding how the various physical processes interplay in the very final stages of star formation. This also affects our capabilities of quantifying photon escape from the dense star forming regions. It is reasonable to think that in realistic conditions the inner cores will be optically thick and only after the photons will have heated up the cloud and thermalized with it they will be able to escape and dissociate molecules in the diffuse IGM. Definitive answers on this topics are still lacking, though. Furthermore, these many uncertainties even lead to differences of several orders of magnitude when comparing mass estimates of haloes affected by radiation (e.g. Ciardi et al. 2000; Kitayama et al. 2001; Dijkstra et al. 2004).

## 5 SUMMARY AND CONCLUSIONS

Cosmic gas and star forming processes are fundamental keywords in modern Astrophysics. They are, however, very complicated to study because they lie in the highly non-linear regime. Thus, simple perturbative approaches do not give relevant information about gas collapse and baryonic-structure growth. To understand them better, it is crucial to consider all the involved physical and chemical mechanisms. In case of early structure formation, primordial chemistry has to be taken into account, since it is mainly via H-derived molecules that first objects can aggregate gas and form stars. Furthermore, it is also necessary to self-consistently include the RT of the photons produced by stellar sources. Indeed,

these travel into the cosmic medium and can ionize the surrounding gas or dissociate formed molecules. As the impacts of RT on the chemical evolution of the early Universe are expected to be significant, it is important to couple such calculations in order to get a reliable picture.

In this work, we have presented numerical methods of coupled chemistry treatment and multi-frequency RT, applied to N-body, hydrodynamical simulations. We used the SPH code GADGET3 – an extended version of the publicly available code GADGET2 (Springel 2005) – including the RT implementation of Petkova & Springel (2009), and the non-equilibrium chemistry implementation of Maio et al. (2007), following  $e^-$ , H,  $H^+$ ,  $H^-$ , He,  $He^+$ ,  $He^{++}$ ,  $H_2$ ,  $H_2^+$ , D,  $D^+$ , HD,  $HeH^+$ .

After a detailed description of the coupling between the RT treatment (Sect. 2.1) and the non-equilibrium chemical treatment (Sect. 2.2), we have performed convergence tests (Sect. 3) and cosmological applications (Sect. 4) of our code.

We have started (in Sect. 3.1) with the expansion of an ionized sphere around a stellar-type source emitting at a temperature of  $\sim 3 \times 10^4$  K in a uniform-density gas. We have traced the element and molecule evolution with time and compared to analytical results (in Fig. 2 and Fig. 3). We found that analytical analyses based on H-only gas at a constant temperature give a sufficient criterion to predict the evolution of the I-front. The different species reach different ionization radii: we use the Strömgen radius defined for H-only gas at  $10^4$  K, as a reference. Deuterium species recombine at a radius comparable (within 10 per cent) to the Strömgen radius, while He gets completely neutral at  $\sim 2/5$  the Strömgen radius.  $H_2$  has an ionization radius that is typically larger than the Strömgen radius of about 40 per cent ( $\sim 7$  kpc vs  $\sim 5$  kpc). The compression of gas due to the propagating I-front enhances molecular species ( $H_2$  and HD) in the outer layers, where temperatures are around  $\sim 10^3 - 10^4$  K. The high values of the creation rates in these temperature regimes make  $H_2$  increase of a few orders of magnitude and HD, as well.

The second test (see Sect. 3.2) is a mean-density cosmological evolution, where the CMB was assumed to be the only source of ionizing radiation. We found that (Fig. 6), because of the low cosmic background emission, the CMB does not affect significantly the abundance evolution, even when considering photon propagation at very-high redshift.

As applications of the numerical methods previously described, we have studied (Sect. 4) the effects of RT on chemical evolution of primordial gas (e.g. Fig. 7). We performed cosmological simulations of structure formation with and without ionizing radiation from stellar sources, and checked the consequences for molecule formation and destruction.

We found that the presence of ionizing radiation from stars depletes molecular hydrogen up to several orders of magnitude (see Fig. 8), by inhibiting the main formation paths (the  $H^-$ -channel and the  $H_2^+$ -channel) and by dissociating it via Lyman-Werner radiation. Our results are consistent with other studies, e.g. Wise & Abel (2007); Johnson et al. (2007); Ahn et al. (2009); Trenti & Stiavelli (2009); Whalen et al. (2010); Latif et al. (2011), who studied the impacts of the UV background in destroying down the  $H_2$  molecule. In addition, we found that also other molecules

formed in pristine gas, like e.g. HD, are strongly suppressed by radiative feedback (Fig. 9).

There are large discrepancies in the quantitative assessments of the impacts of radiative feedback on baryonic structure formation in the current literature. In fact, different works (e.g. Ciardi et al. 2000; Dijkstra et al. 2004) show uncertainties of several orders of magnitudes on the basic estimates of the masses of the haloes affected by radiation. Such determinations could even be highly biased by their different “post-processing” approaches. Indeed, in order to have large statistics or to circumvent numerical complications, these studies do not consider hydrodynamics self-consistently coupled with RT and non-equilibrium chemistry. That could be problematic for getting to reliable conclusions, since, as shown by our numerical simulations (Sect. 4), RT effects on gas evolution could be quite important and affect star forming regions in a non-negligible way. The destruction of early molecules by stellar sources has a deep impact on the following star formation processes, because it hinders the successive birth of metal-free stars. This also implies the need of different viable low-temperature coolants, like metals (e.g. Maio et al. 2007), or the presence of reionized gas (Yoshida et al. 2007) to sustain star formation at later times. The obvious expectation is, then, that the popIII star formation rate will drop (even more heavily than expected by Maio et al. 2010, 2011; Hasegawa et al. 2009; Tornatore et al. 2007; O’Shea & Norman 2008b; Johnson & Khochfar 2011). However, further and more detailed investigations of high-resolution, numerical simulations are required to draw final and definitive conclusions on this topic.

## ACKNOWLEDGMENTS

We acknowledge useful discussions with Benedetta Ciardi, Mark Dijkstra, Klaus Dolag, Edoardo Tescari, Dan Whalen. The analysis and the simulations have been performed on the MPA AMD Opteron machines at the Garching Computing Center (Rechenzentrum Garching, RZG). This research has made use of NASA’s Astrophysics Data System and of the JSTOR Archive.

## REFERENCES

- Abel T., Anninos P., Zhang Y., Norman M. L., 1997, *New Astronomy*, 2, 181
- Abel T., Bryan G. L., Norman M. L., 2002, *Science*, 295, 93
- Ahn K., Shapiro P. R., 2007, *MNRAS*, 375, 881
- Ahn K., Shapiro P. R., Iliev I. T., Mellema G., Pen U.-L., 2009, *ApJ*, 695, 1430
- Alvarez M. A., Bromm V., Shapiro P. R., 2006, *ApJ*, 639, 621
- Anninos P., Zhang Y., Abel T., Norman M. L., 1997, *New Astronomy*, 2, 209
- Bishop D. M., Cheung L. M., 1979, *Journal of Molecular Spectroscopy*, 75, 462
- Black J. H., 1981, *MNRAS*, 197, 553
- Bromm V., Coppi P. S., Larson R. B., 2002, *ApJ*, 564, 23
- Bromm V., Loeb A., 2003, *Nature*, 425, 812



- Campisi M. A., Maio U., Salvaterra R., Ciardi B., 2011, *MNRAS*, 416, 2760
- Campisi M. A., Tapparello C., Salvaterra R., Mannucci F., Colpi M., 2011, *MNRAS*, 417, 1013
- Cen R., 1992, *ApJS*, 78, 341
- Ciardi B., Ferrara A., 2005, *Space Science Review*, 116, 625
- Ciardi B., Ferrara A., Abel T., 2000, *ApJ*, 533, 594
- Ciardi B., Ferrara A., Governato F., Jenkins A., 2000, *MNRAS*, 314, 611
- Ciardi B., Ferrara A., Marri S., Raimondo G., 2001, *MNRAS*, 324, 381
- Croft R. A. C., Altay G., 2008, *MNRAS*, 388, 1501
- de Souza R. S., Yoshida N., Ioka K., 2011, *A&A*, 533, A32+
- Desjacques V., Seljak U., Iliev I. T., 2009, *MNRAS*, 396, 85
- Dijkstra M., Haiman Z., Rees M. J., Weinberg D. H., 2004, *ApJ*, 601, 666
- Draine B. T., Bertoldi F., 1996, *ApJ*, 468, 269
- Efstathiou G., 1992, *MNRAS*, 256, 43P
- Galli D., Palla F., 1998, *A&A*, 335, 403
- Glover S. C. O., Abel T., 2008, *MNRAS*, 388, 1627
- Glover S. C. O., Brand P. W. J. L., 2003, *MNRAS*, 340, 210
- Glover S. C. O., Federrath C., Mac Low M.-M., Klessen R. S., 2010, *MNRAS*, 404, 2
- Gnedin N. Y., Abel T., 2001, *New Astronomy*, 6, 437
- Gnedin N. Y., Tassis K., Kravtsov A. V., 2009, *ApJ*, 697, 55
- Greif T. H., White S. D. M., Klessen R. S., Springel V., 2011, *ApJ*, 736, 147
- Grinstein B., Wise M. B., 1986, *ApJ*, 310, 19
- Grossi M., Dolag K., Branchini E., Matarrese S., Moscardini L., 2007, *MNRAS*, 382, 1261
- Haardt F., Madau P., 1996, *ApJ*, 461, 20
- Haiman Z., 1999, *Ap&SS*, 269, 191
- Haiman Z., Rees M. J., Loeb A., 1997a, *ApJ*, 476, 458
- Haiman Z., Rees M. J., Loeb A., 1997b, *ApJ*, 484, 985
- Haiman Z., Rees M. J., Loeb A., 1997c, *ApJ*, 484, 985
- Hasegawa K., Umemura M., Susa H., 2009, *MNRAS*, 395, 1280
- Hui L., Gnedin N. Y., 1997a, *MNRAS*, 292, 27
- Hui L., Gnedin N. Y., 1997b, *MNRAS*, 292, 27
- Iliev I. T., Ciardi B., Alvarez M. A., Maselli A., Ferrara A., Gnedin N. Y., Mellema G., Nakamoto T., Norman M. L., Razoumov A. O., Rijkhorst E.-J., Ritzerveld J., Shapiro P. R., Susa H., Umemura M., Whalen D. J., 2006, *MNRAS*, 371, 1057
- Iliev I. T., Shapiro P. R., Raga A. C., 2005, *MNRAS*, 361, 405
- Iliev I. T., Whalen D., Mellema G., Ahn K., Baek S., Gnedin N. Y., Kravtsov A. V., Norman M., Raicevic M., Reynolds D. R., Sato D., Shapiro P. R., Semelin B., Smidt J., Susa H., Theuns T., Umemura M., 2009, *MNRAS*, 400, 1283
- Jeans J. H., 1902, *Phil. Trans.*, 199, A p.1+
- Johnson J. L., Greif T. H., Bromm V., 2007, *ApJ*, 665, 85
- Johnson J. L., Khochfar S., 2011, *MNRAS*, 413, 1184
- Karpas Z., Anicich V., Huntress Jr. W. T., 1979, *J. Chem. Phys.*, 70, 2877
- Kitayama T., Susa H., Umemura M., Ikeuchi S., 2001, *MNRAS*, 326, 1353
- Komatsu E., Smith K. M., Dunkley J., 18 coauthors 2011, *ApJS*, 192, 18
- Komatsu E., Wandelt B. D., Spergel D. N., Banday A. J., Górski K. M., 2002, *ApJ*, 566, 19
- Koyama K., Soda J., Taruya A., 1999, *MNRAS*, 310, 1111
- Latif M. A., Schleicher D. R. G., Spaans M., Zaroubi S., 2011, *A&A*, 532, A66+
- Lepp S., Shull J. M., 1984, *ApJ*, 280, 465
- Lipovka A., Núñez-López R., Avila-Reese V., 2005, *MNRAS*, 361, 850
- Machacek M. E., Bryan G. L., Abel T., 2001, *ApJ*, 548, 509
- Machacek M. E., Bryan G. L., Abel T., 2003, *MNRAS*, 338, 273
- Mackey J., Bromm V., Hernquist L., 2003, *ApJ*, 586, 1
- Maio U., 2011, *Classical and Quantum Gravity*, 28, 225015
- Maio U., Ciardi B., Dolag K., Tornatore L., Khochfar S., 2010, *MNRAS*, 407, 1003
- Maio U., Ciardi B., Yoshida N., Dolag K., Tornatore L., 2009, *A&A*, 503, 25
- Maio U., Dolag K., Ciardi B., Tornatore L., 2007, *MNRAS*, 379, 963
- Maio U., Dolag K., Meneghetti M., Moscardini L., Yoshida N., Baccigalupi C., Bartelmann M., Perrotta F., 2006, *MNRAS*, 373, 869
- Maio U., Iannuzzi F., 2011, *MNRAS*, 415, 3021
- Maio U., Khochfar S., 2012, *MNRAS*, p. 2250
- Maio U., Khochfar S., Johnson J. L., Ciardi B., 2011, *MNRAS*, 414, 1145
- Maio U., Koopmans L. V. E., Ciardi B., 2011, *MNRAS*, 412, L40
- Mellema G., Iliev I. T., Alvarez M. A., Shapiro P. R., 2006, *New Astronomy*, 11, 374
- Mesinger A., Bryan G. L., Haiman Z., 2006, *ApJ*, 648, 835
- Mesinger A., Bryan G. L., Haiman Z., 2009, *MNRAS*, 399, 1650
- Nakamura F., Umemura M., 2002, *ApJ*, 569, 549
- Neufeld D. A., Dalgarno A., 1989, *ApJ*, 340, 869
- Omukai K., Hosokawa T., Yoshida N., 2010, *ApJ*, 722, 1793
- Omukai K., Nishi R., 1999, *ApJ*, 518, 64
- Omukai K., Tsuribe T., Schneider R., Ferrara A., 2005, *ApJ*, 626, 627
- O'Shea B. W., Norman M. L., 2008a, *ApJ*, 673, 14
- O'Shea B. W., Norman M. L., 2008b, *ApJ*, 673, 14
- Paardekooper J.-P., Pelupessy F. I., Altay G., Kruip C. J. H., 2011, *A&A*, 530, A87+
- Pawlik A. H., Schaye J., 2011, *MNRAS*, 412, 1943
- Peterson J. R., Aberth W. H., Moseley J. T., Sheridan J. R., 1971, *Phys. Rev. A*, 3, 1651
- Petkova M., Springel V., 2009, *MNRAS*, 396, 1383
- Petkova M., Springel V., 2011, *MNRAS*, 412, 935
- Puy D., Alecian G., Le Bourlot J., Leorat J., Pineau Des Forets G., 1993, *A&A*, 267, 337
- Ricotti M., Gnedin N. Y., Shull J. M., 2001, *ApJ*, 560, 580
- Ricotti M., Gnedin N. Y., Shull J. M., 2002a, *ApJ*, 575, 33
- Ricotti M., Gnedin N. Y., Shull J. M., 2002b, *ApJ*, 575, 49
- Roberge W., Dalgarno A., 1982, *ApJ*, 255, 489
- Saslaw W. C., Zipoy D., 1967, *Nature*, 216, 976
- Savin D. W., 2002, *ApJ*, 566, 599
- Savin D. W., Krstić P. S., Haiman Z., Stancil P. C., 2004, *ApJ*, 606, L167

- Schneider R., Ferrara A., Salvaterra R., Omukai K., Bromm V., 2003, *Nature*, 422, 869
- Schneider R., Omukai K., Bianchi S., Valiante R., 2012, *MNRAS*, 419, 1566
- Schwarzschild M., Spitzer L., 1953, *The Observatory*, 73, 77
- Shang C., Bryan G. L., Haiman Z., 2010, *MNRAS*, 402, 1249
- Shapiro P. R., Iliev I. T., Raga A. C., 2004, *MNRAS*, 348, 753
- Shapiro P. R., Kang H., 1987a, *ApJ*, 318, 32
- Shapiro P. R., Kang H., 1987b, *ApJ*, 318, 32
- Smith B. D., Turk M. J., Sigurdsson S., O'Shea B. W., Norman M. L., 2009, *ApJ*, 691, 441
- Spitzer L., 1962, *Physics of Fully Ionized Gases*, New York: Interscience (2nd edition), 1962. Spitzer L.
- Spitzer L., 1978, *Physical processes in the interstellar medium*. Spitzer, L.
- Springel V., 2005, *MNRAS*, 364, 1105
- Stacy A., Bromm V., Loeb A., 2011, *ApJ*, 730, L1+
- Stacy A., Greif T. H., Bromm V., 2011, *arXiv:astro-ph/1109.314*
- Stancil P. C., Lepp S., Dalgarno A., 1998, *ApJ*, 509, 1
- Stibbe D. T., Tennyson J., 1999, *ApJ*, 513, L147
- Susa H., 2007, *ApJ*, 659, 908
- Susa H., Umemura M., 2004, *ApJ*, 600, 1
- Susa H., Umemura M., 2006, *ApJ*, 645, L93
- Susa H., Umemura M., Hasegawa K., 2009, *ApJ*, 702, 480
- Thoul A. A., Weinberg D. H., 1996, *ApJ*, 465, 608
- Tornatore L., Ferrara A., Schneider R., 2007, *MNRAS*, 382, 945
- Trenti M., Stiavelli M., 2009, *ApJ*, 694, 879
- Tseliakhovich D., Hirata C., 2010, *Phys. Rev. D*, 82, 083520
- Uehara H., Inutsuka S.-i., 2000, *ApJ*, 531, L91
- Wang J. G., Stancil P. C., 2002, *Physica Scripta*, T96, 1, 72
- Whalen D., Abel T., Norman M. L., 2004, *ApJ*, 610, 14
- Whalen D., Hueckstaedt R. M., McConkie T. O., 2010, *ApJ*, 712, 101
- Whalen D., Norman M. L., 2008, *ApJ*, 673, 664
- Whalen D., van Veelen B., O'Shea B. W., Norman M. L., 2008, *ApJ*, 682, 49
- Wise J. H., Abel T., 2007, *ApJ*, 671, 1559
- Wise J. H., Abel T., 2008, *ApJ*, 685, 40
- Wolcott-Green J., Haiman Z., Bryan G. L., 2011, *MNRAS*, p. 1673
- Yoshida N., Abel T., Hernquist L., Sugiyama N., 2003, *ApJ*, 592, 645
- Yoshida N., Oh S. P., Kitayama T., Hernquist L., 2006, *arXiv:astro-ph/0610819*
- Yoshida N., Oh S. P., Kitayama T., Hernquist L., 2007, *ApJ*, 663, 687
- Yoshida N., Omukai K., Hernquist L., Abel T., 2006, *ApJ*, 652, 6